

Article

Idealized Simulations of a Supercell Interacting with an Urban Area

Jason Naylor *, Megan E. Berry and Emily G. Gosney

Department of Geographic and Environmental Sciences, University of Louisville, Louisville, KY 40292, USA; meg.cooper@louisville.edu (M.E.B.); emily.gosney@louisville.edu (E.G.G.)

* Correspondence: jason.naylor@louisville.edu

Abstract: Idealized simulations with a cloud-resolving model are conducted to examine the impact of a simplified city on the structure of a supercell thunderstorm. The simplified city is created by enhancing the surface roughness length and/or surface temperature relative to the surroundings. When the simplified city is both warmer and has larger surface roughness relative to its surroundings, the supercell that passes over it has a larger updraft helicity (at both midlevels and the surface) and enhanced precipitation and hail downwind of the city, all relative to the control simulation. The storm environment within the city has larger convective available potential energy which helps stimulate stronger low-level updrafts. Storm relative helicity (SRH) is actually reduced over the city, but enhanced in a narrow band on the northern edge of the city. This band of larger SRH is ingested by the primary updraft just prior to passing over the city, corresponding with enhancement to the near-surface mesocyclone. Additional simulations in which the simplified city is altered by removing either the heat island or surface roughness length gradient reveal that the presence of a heat island is most closely associated with enhancements in updraft helicity and low-level updrafts relative to the control simulation.

Keywords: supercell; convection; idealized; urban



Citation: Naylor, J.; Berry, M.E.; Gosney, E.G. Idealized Simulations of a Supercell Interacting with an Urban Area. *Meteorology* **2024**, *3*, 97–113. <https://doi.org/10.3390/meteorology3010005>

Academic Editors: Edoardo Bucchignani, Andrea Mastellone and Paul D. Williams

Received: 18 December 2023
Revised: 8 February 2024
Accepted: 23 February 2024
Published: 7 March 2024



Copyright: © 2024 by the authors. Licensee MDPI, Basel, Switzerland. This article is an open access article distributed under the terms and conditions of the Creative Commons Attribution (CC BY) license (<https://creativecommons.org/licenses/by/4.0/>).

1. Introduction

Supercells are some of the most intense thunderstorms on Earth. These rotating thunderstorms are not only responsible for the vast majority of strong tornadoes, but nearly all large hail events as well [1]. They can also produce damaging straight-line winds and flash flooding. Because of the societal hazards associated with these storms, timely and accurate prediction is key. While the overall environmental conditions responsible for supercell formation are well known [2–5], many studies have found that gradients (or boundaries) in the mesoscale environment can have a substantial impact on the supercell structure and evolution [6–13].

In addition to gradients in atmospheric properties, supercells have also been found to be influenced by variability in land surface characteristics, particularly terrain [14–17]. Some studies have also noted that tornado development in supercells may be impacted by elevation changes [18–22] while others have explored the link between tornado formation and variations in surface roughness [22–24]. Numerical simulations have also shown that the development of near-ground rotation is sensitive to surface friction magnitude [25–27].

Another well-known factor that has been shown to impact thunderstorms is the presence of an urban area [28–30]. Urban areas can contain gradients in both atmospheric properties (due to the urban heat island) and surface roughness characteristics (due to the horizontal variations in land use). While many studies have shown that large cities can influence a thunderstorm structure [31], only a few have investigated organized forms of convection [32,33]. Recently, Naylor and Mulholland [33] (herein NM23) conducted the idealized simulations of squall lines interacting with a simplified urban area. Under

moderate-to-strong low-level wind shear in the storm environment, mid-level updrafts were enhanced after passing over the idealized city with the magnitude of the enhancement being strongly dependent on the strength of the urban heat island. Trajectory analysis revealed that updraft parcels originating from the urban area had increased buoyancy resulting in stronger vertical motion. In contrast, weak wind shear produced updrafts with a rearward tilt. In these simulations, parcels with enhanced buoyancy were confined to the low-level updraft, which resulted in an amplified front-to-rear pressure gradient that accelerated the rear inflow jet. Furthermore, very few studies have specifically examined the interactions between supercells and urban areas [34,35]. Reames and Stensrud [34] conducted real-data simulations with the Weather Research and Forecasting (WRF) model and found that the presence of an urban area modified the mid-level and low-level rotational properties of a supercell. However, they did not note any impacts to updraft strength. Lin et al. [35] also used a version of the WRF model to simulate a supercell near Kansas City, MO. While Lin et al. [35] did note that the presence of an urban area resulted in a stronger updraft, they did not examine the rotational properties of the supercell. In addition, neither of the aforementioned studies examined the relative influence of temperature and roughness anomalies over the urban areas. The purpose of this study is to further examine the interactions between supercells and urban areas in a controlled, idealized framework to understand how spatial gradients in temperature and surface roughness length can impact the storm structure with an emphasis on the development on low-level rotation.

2. Methodology

Cloud Model 1 (CM1) version 18 [36] is used for all simulations. The model is configured with a constant horizontal grid spacing of 250 m and a stretched vertical grid. The horizontal domain is 240 km in both the east–west and north–south directions. The vertical grid spacing is 50 m below $z = 2.4$ km and stretches to 500 m by $z = 9$ km. A total of 98 vertical levels are used and the model top is 22 km. While the horizontal grid spacing is not sufficient to fully resolve simulated tornadoes, it is sufficient to resolve the storm-scale processes that promote the development of near-surface rotation [37–39]. Microphysical processes are represented by the double-moment scheme from [40,41], with hail set as the prognostic ice species. Simulations are run for 3.5 h and model history files are output every 5 min for the first 90 min of the simulation time and every 1 min afterward. Open-radiative boundary conditions are used in the horizontal directions. A free slip upper-boundary condition is used with Rayleigh damping applied above $z = 15$ km. The lower boundary is semi-slip. The surface drag is based on [42] for small wind speeds and [43] for large wind speeds.

Figure 1 shows a skew-T diagram and hodograph of the initial conditions, which are based on the thermodynamic profile from [2,3] and quarter-circle hodograph from [44]. These conditions produce a storm environment with a CAPE of approximately 2200 J kg^{-1} and a 0–6 km bulk wind shear of 32 m s^{-1} . Storm relative helicity is $81 \text{ m}^2 \text{ s}^{-2}$ over the 0–1 km layer and $192 \text{ m}^2 \text{ s}^{-2}$ over the 0–3 km layer. Storms are initiated using a thermal bubble with a maximum potential temperature perturbation of 1.5 K placed in the western side of the domain at the initial time step. The location of the thermal bubble is chosen such that the primary updraft of the mature right-moving supercell passes through the center of the domain in both the x and y directions. The bubble is centered 1.4 km above the lower boundary with a vertical radius of 1.4 km and a 10 km horizontal radius. Random potential temperature perturbations with a maximum magnitude of 0.25 K are inserted into the initial conditions.

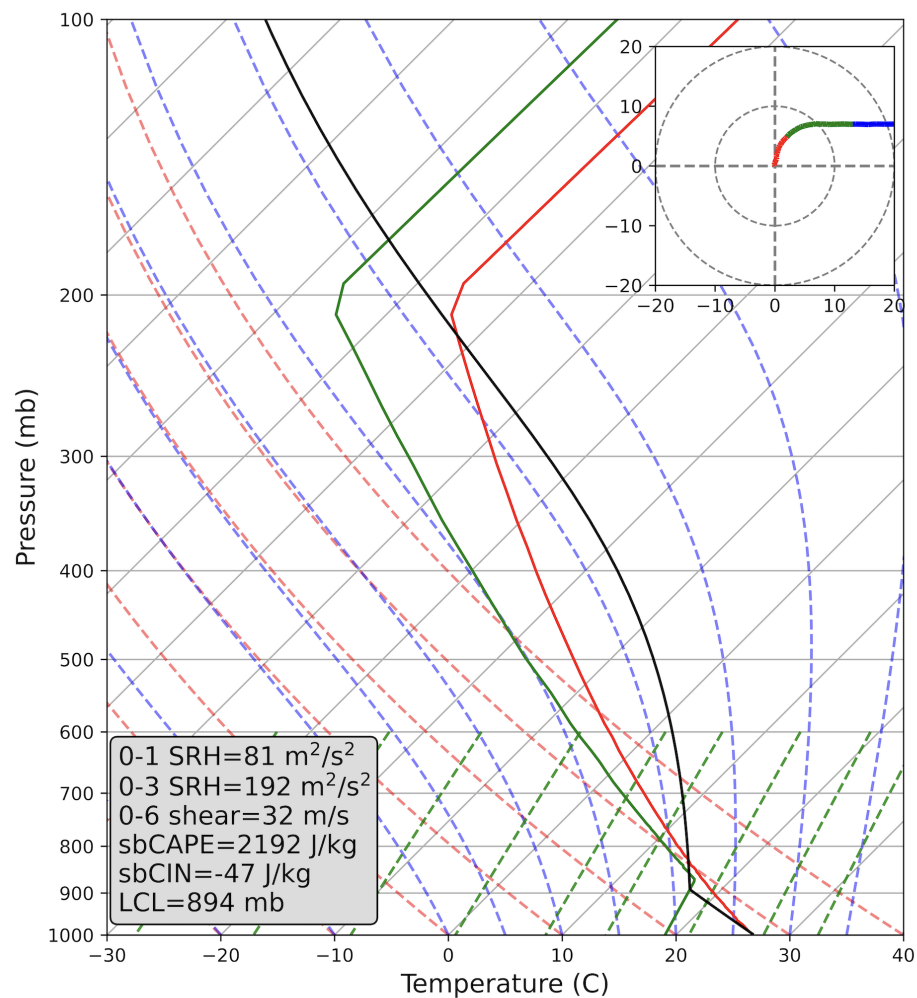


Figure 1. Skew-T log-p diagram and hodograph (inset) of the initial conditions. The hodograph has units of m s^{-1} and is colored by height above the surface. Red represents horizontal winds between 0 and 1 km, green between 1 and 3 km, and blue from 3 to 10 km. The box in the lower-left of the skew-T diagram contains calculated parameters such as 0–1 km storm relative helicity (0–1 SRH), 0–3 km storm relative helicity (0–3 SRH), 0–6 km bulk wind shear magnitude (0–6 shear), convective available potential energy for a surface-based parcel (sbCAPE), convective inhibition for a surface-based parcel (sbCIN), and the lifting condensation level of a surface-based parcel (LCL).

In the control simulation, the surface has a constant skin temperature of 300 K and a roughness length of 0.2 m, which is representative of a mixture of cropland and woodland. All other surface characteristics (e.g., moisture availability, thermal inertia) are chosen such that the low-level thermal structure remains approximately constant over the duration of the simulation. A second simulation includes a simplified urban area which is placed in the center of the model domain (herein simply referred to as the “city” simulation). To approximate urban effects, the methodology of NM23 is used: a circular region with a radius of 10 km is placed in the center of the domain. Within this region, the skin temperature is 5 K greater than the surroundings and the surface roughness length is set to 2 m, which is comparable to the roughness length of the center of a very dense urban area containing high-rise buildings. Testing has shown that a 5 K skin temperature excess in combination with a 2 m roughness length is the largest possible without new convective cells being initiated on the edge of the city in this particular model configuration. Naylor [32] and NM23 have shown that, for a given skin temperature excess, increasing the surface roughness length results in stronger and deeper heat islands due to increased vertical mixing.

Although some recent studies have utilized a force-balance procedure to ensure that the environmental wind profile remains steady throughout the simulation [26], no such balancing procedure is used in the current study. Table 1 shows values of environmental parameters at a grid point downwind of the domain center at three different times. Storm relative helicity is an integrated parameter that is sensitive to small changes in wind speed and direction. Over the first 90 min, there is little change to SRH. Thermodynamic fields such as CAPE, CIN, and LCL height are sensitive to surface temperature and moisture and these fields also show minimal fluctuations.

While the environment is quasi-steady away from the domain center, the presence of a heat island in the city simulation has a strong impact on the near-surface thermodynamic structure (Figure 2) Temperature differences between the city and the surrounding area extend to at least 525 m above the surface. The heat island is strongest near the surface and reaches a peak magnitude between $t = 80$ min and $t = 100$ min. After this time, the heat island magnitude decreases sharply as the cold pool from the supercell passes over the simplified city.

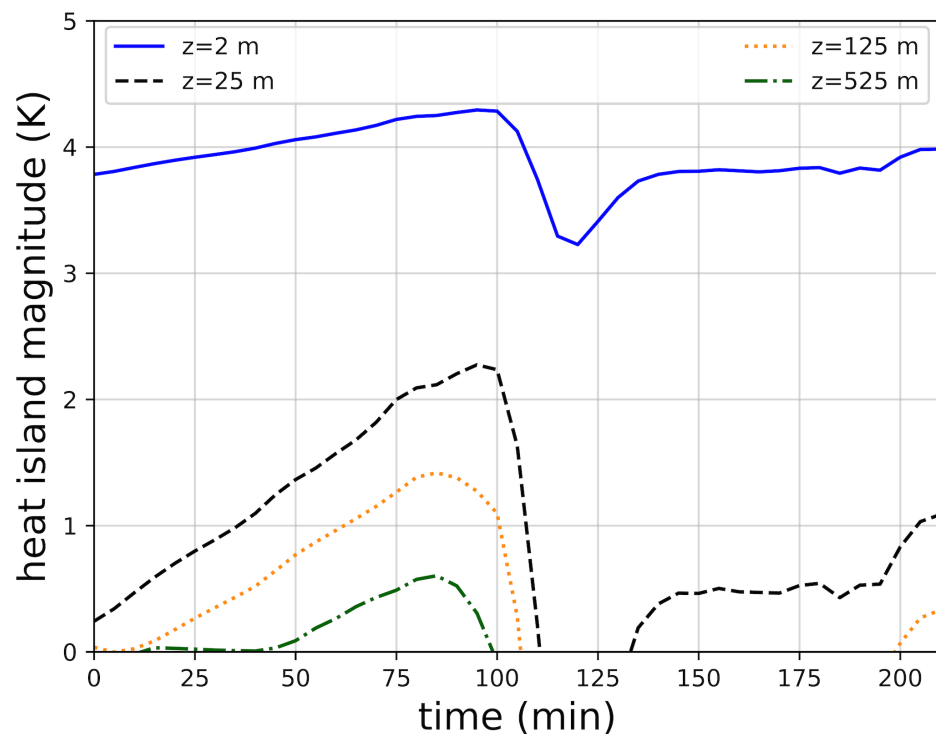


Figure 2. The time-series of heat island magnitude at different vertical levels in the city simulation. Heat island magnitude is calculated as the difference between the average temperature within the idealized city at a particular level and the temperature of the far field at the same level.

Additional simulations are also presented for comparison to the control and city simulations. In one simulation (herein referred to as the “noUHI” simulation) the simplified city does not produce a heat island but still represents an area of enhanced surface roughness length. In another simulation, (herein referred to as “no Δz_0 ”), a heat island is present but the surface roughness length is not enhanced over the simplified city. Because heat island depth and magnitude are sensitive to the turbulence induced by the enhanced surface roughness, a 10 K skin temperature perturbation was needed in the no Δz_0 simulation to generate a heat island similar to that found in the city simulation. Several additional sensitivity tests are performed to verify the robustness of the results. In these simulations—the details of which are given in the next section—a small ensemble is created by varying physics parameterizations and shifting the initial location of the warm bubble perturbation.

Table 1. Values of environmental parameters at a grid point 40 km west of the domain center at three select times. Values on the left of each cell are for the control simulation and values in parentheses are for the city simulation.

Parameter	$t = 30 \text{ min}$	$t = 60 \text{ min}$	$t = 90 \text{ min}$
0–1 SRH ($\text{m}^2 \text{s}^{-2}$)	75 (75)	81 (81)	82 (82)
0–3 SRH ($\text{m}^2 \text{s}^{-2}$)	187 (187)	192 (192)	192 (192)
0–6 shear (m s^{-1})	32 (32)	32 (32)	32 (32)
sbCAPE (J kg^{-1})	2165 (2165)	2198 (2198)	2087 (2081)
sbCIN (J kg^{-1})	−49 (−49)	−49 (−49)	−51 (−51)
LCL (mb)	894 (894)	894 (894)	894 (894)

3. Results

Over the first 80 min of the simulation time, the two simulations are practically identical (Figure 3). The warm bubble initiation method causes a storm to grow and eventually form a splitting supercell with the right-moving storm moving across the center of the domain (not shown). By $t = 90 \text{ min}$, small differences in vertical velocity begin to emerge due to the storm in the city simulation approaching and interacting with the simplified city. The cold pool from the right-moving supercell in both simulations passes over the domain center around $t = 100 \text{ min}$ (Figure 2).

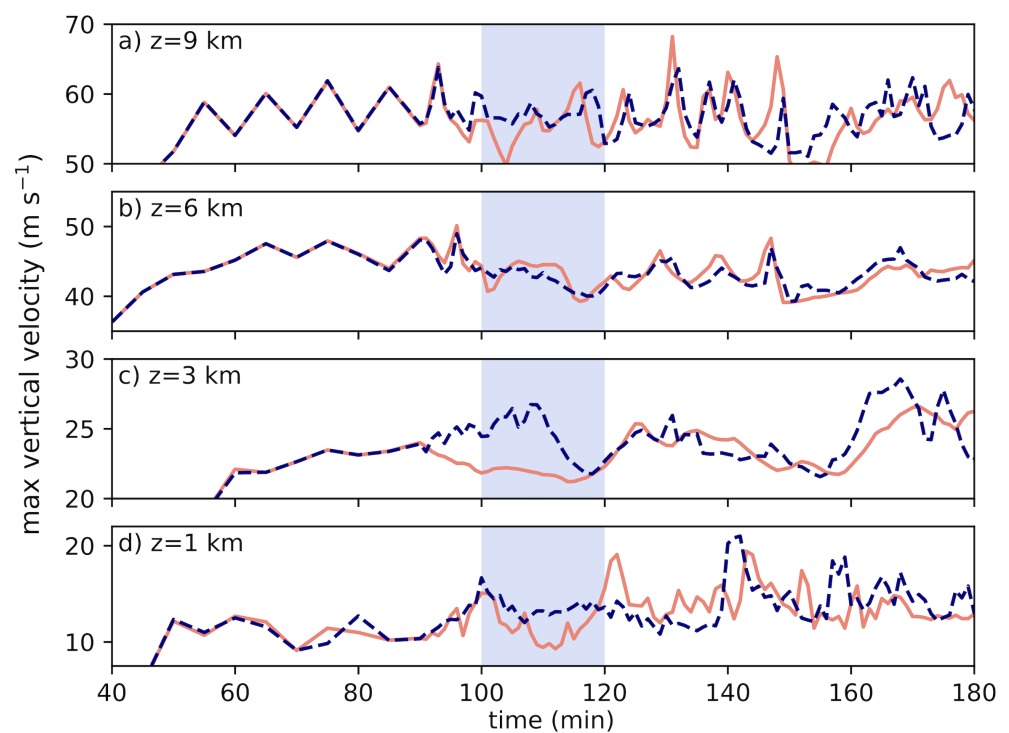


Figure 3. Time-series of maximum vertical velocity for the city (blue-dashed line) and control (orange solid line) simulations at vertical grid levels approximately (a) $z = 9 \text{ km}$, (b) $z = 6 \text{ km}$, (c) $z = 3 \text{ km}$, and (d) $z = 1 \text{ km}$ above the lower boundary. Data prior to $t = 90 \text{ min}$ have a temporal resolution of 5 min, with a 1 min resolution after $t = 90 \text{ min}$. The blue box highlights the approximate time period that the updraft of the right moving supercell passes over the defined urban area in the center of the domain.

At mid- to upper levels (Figure 3a,b), the two simulations exhibit minimal differences in vertical velocity. The largest differences are found at lower levels and are coincident with interactions between the supercell updraft and simplified city (Figure 3c,d). Around $t = 90 \text{ min}$, vertical velocity at $z = 3 \text{ km}$ in the control simulation begins to decrease. In contrast, the supercell in the city simulation experiences a steady increase in vertical velocity at $z = 3 \text{ km}$ as it approaches the western edge of the idealized city. This continues until

approximately $t = 110$ min when the maximum 3 km vertical velocity in the city simulation reaches 27 m s^{-1} compared to 22 m s^{-1} in the control simulation at the same time. After this time, 3 km vertical velocity in the two supercells is quite similar for the remainder of the simulations. Differences in vertical velocity can also be seen at $z = 1$ km (Figure 3d). From $t = 100$ min through $t = 110$ min values of maximum vertical velocity at $z = 1$ km in the city simulation are more consistent than those in the control simulation, which experiences sudden decreases in vertical velocity during this period. At $t = 110$ min, the maximum $z = 1$ km vertical velocity in the city simulation is 13 m s^{-1} , but only 10 m s^{-1} in the control simulation. Another noticeable difference can be seen around $t = 120$ min, with the supercell in the control simulation experiencing a sudden but short-lived increase in vertical velocity that is not present in the city simulation. Although this peak is short-lived, vertical velocity at $z = 1$ km remains slightly stronger in the control simulation until approximately $t = 140$ min.

The strength of the mesocyclone can be quantified by updraft helicity (UH), which represents the product of vertical velocity (w) and vertical vorticity (ζ) integrated from a lower height (z_1) to an upper height (z_2)

$$UH = \int_{z_1}^{z_2} w\zeta dz \tag{1}$$

For the midlevel mesocyclone, 2–5 km has been shown to be an appropriate integration depth [45–47] while the near-surface mesocyclone can be represented by UH integrated from 0 to 1 km [48].

The tracks of the midlevel and surface mesocyclones are shown in Figure 4a–d. The midlevel mesocyclone tracks across the center of the domain in both the control and city simulations (Figure 4a,b). In the city simulation, this means that the mesocyclone passes directly through the idealized city. In the control simulation, the midlevel mesocyclone reaches a maximum strength near $x = -15$ km (Figure 4a). A similar signature is seen in the city simulation at approximately the same location (Figure 4b). Both mesocyclones experience several brief episodes of intensification as the storms continue to move east and track across the center of the domain. These intensification periods are stronger in magnitude and cover a larger area in the city simulation (Figure 4a,b). Closer to the surface, the low-level mesocyclone is quite weak in the control simulation (Figure 4c). In the center of the domain, there are small, brief increases in UH_{0-1} , but overall the values remain small in magnitude and cover a limited area (Figure 4c). In contrast, UH_{0-1} in the city simulation becomes large just outside the western edge of the idealized city with larger values persisting across the width of the simplified city before decreasing just outside of the eastern edge (Figure 4d). In the city simulation, areas of enhanced UH_{0-1} tracks are closely aligned with the increased vertical vorticity near the surface (Figure 4f).

The time evolution of maximum updraft helicity is impacted by the presence of the city, with differences between the two simulations being more prominent near the surface (Figure 5). At midlevels, UH_{2-5} is identical until approximately $t = 90$ min. Around $t = 98$ min both supercells experience an increase in UH_{2-5} to over $2500 \text{ m}^2 \text{ s}^{-2}$. Over the next 20 min, UH_{2-5} declines in both simulations but a maximum UH_{2-5} in the city simulation remains larger in comparison to the control while passing over the simplified city. After $t = 120$ min, both supercells have comparable patterns in UH_{2-5} . Larger differences are seen in UH_{0-1} (Figure 5b). Between $t = 60$ min and $t = 80$ min, UH_{0-1} in both supercells begins to increase. As the supercell in the city simulation approaches the western edge of the simplified city, UH_{0-1} abruptly jumps to nearly $200 \text{ m}^2 \text{ s}^{-2}$ and remains over $100 \text{ m}^2 \text{ s}^{-2}$ as the primary circulation passes over the simplified city. In contrast, UH_{0-1} in the control simulation remains less than $75 \text{ m}^2 \text{ s}^{-2}$ during this same time period. After $t = 120$ min, at which point the supercell in the city simulation has completely left the simplified city, UH_{0-1} values decrease to those seen in the control simulation. Not only are maximum values of UH_{0-1} greater in the city simulation while the supercell passes over the simplified city, but the overall area of larger UH_{0-1} is amplified as well (Figure 5c). Between $t = 100$

and $t = 120$ min, the area of a larger UH_{0-1} in the city simulation is more than triple that in the control simulation. After this time, the area of UH_{0-1} rapidly decreases in the city simulation and follows a similar pattern to control for the remainder of the simulation.

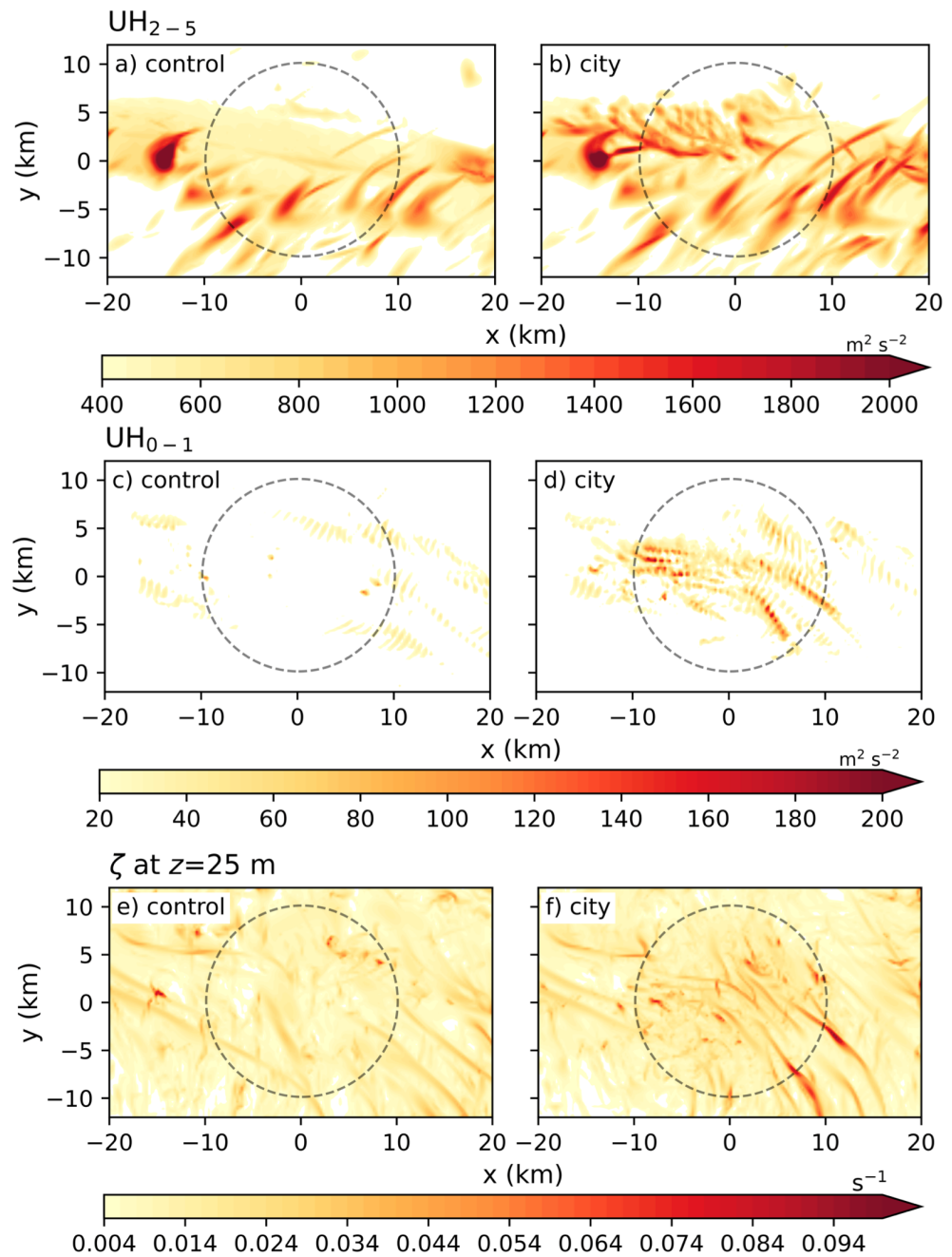


Figure 4. Swaths of 2–5 km updraft helicity (a,b), 0–1 km updraft helicity (c,d), and vertical vorticity (ζ ; e,f) at the lowest model level. The 0–1 km UH values are filtered based on a 2–5 km UH threshold of $150 m^2 s^{-2}$. The dashed gray circle represents the location and extent of the simplified city. For the control simulations (a,c), the areal extent of the simplified city is simply shown for reference.

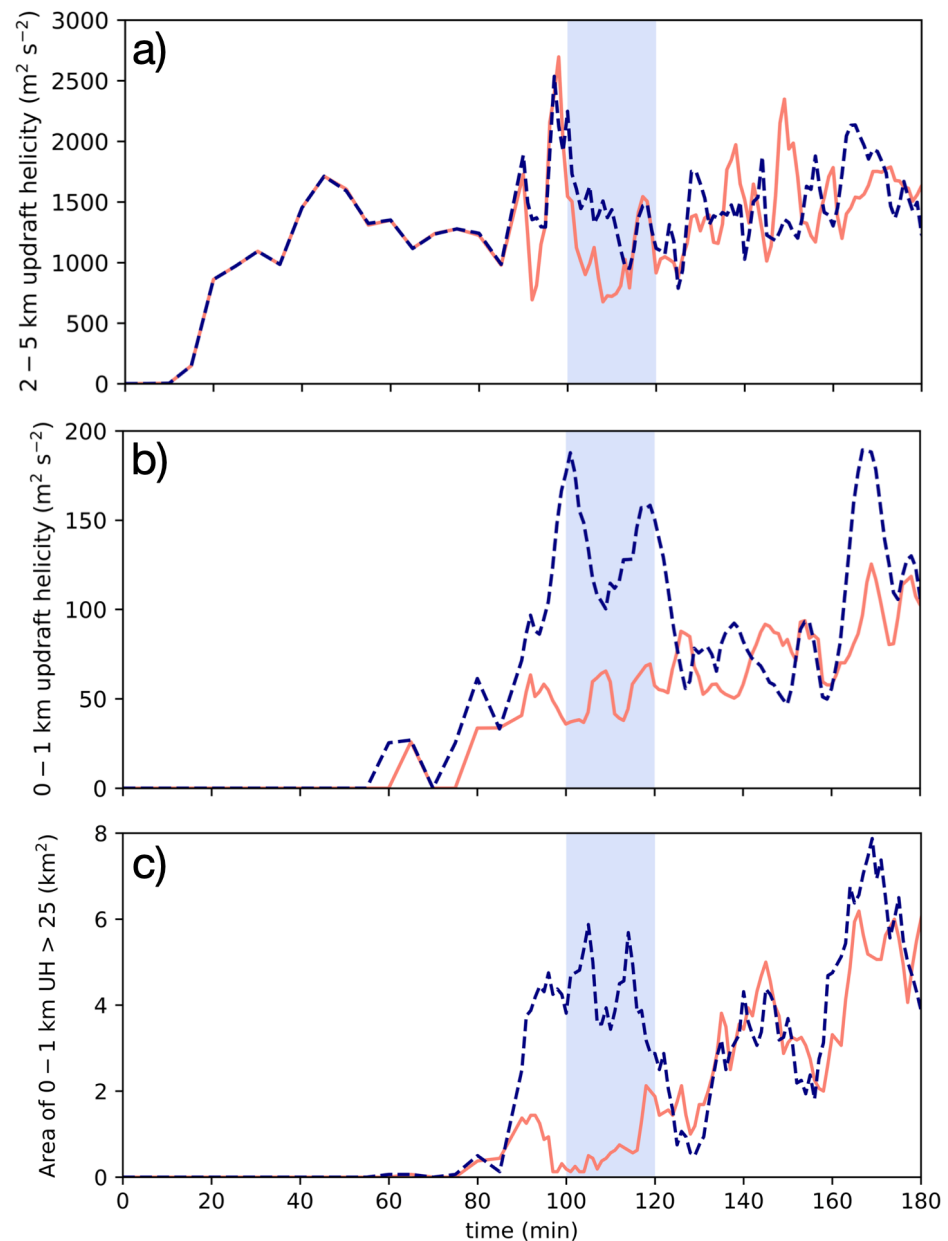


Figure 5. (a) Time-series of grid point maximum 2–5 km UH values in the city (blue dashed line) and control (solid orange line) simulations. The shaded blue area represents the approximate time period that the updraft of the right moving supercells passes over the defined urban area in the center of the domain. Panel (b) is similar to (a), except showing 0–1 km UH. Values after $t = 90$ min are smoothed using a 5 min moving average. Panel (c) shows the time-series of the areal extent of UH_{0-1} greater than $25 \text{ m}^2 \text{ s}^{-2}$ in each simulation. All values in (b,c) are masked to only consider grid points also associated with UH_{2-5} greater than $150 \text{ m}^2 \text{ s}^{-2}$.

The presence of the simplified city has a strong impact on the local storm environment (Figure 6). At $t = 75$ min, the primary updraft is approximately 30 km to the west of the domain center. Low-level flow into the updraft base creates a localized increase in SRH in both simulations (near $x = -25 \text{ km}$, $y = 0 \text{ km}$; Figure 6a,b). In addition, the presence of the simplified city has a noticeable impact on SRH, with reduced values over the city and a narrow ribbon of enhanced SRH on its north side (Figure 6b). The urban heat island within the city also produces a substantial enhancement to CAPE (Figure 6d). The average CAPE over the simplified city is approximately 2700 J kg^{-1} compared to $2100\text{--}2200 \text{ J kg}^{-1}$ in the environment outside of the city. By $t = 90$ min, the forward flank region of the

supercell crosses the domain center in both simulations. In the city simulation, the ribbon of enhanced 0–1 km SRH on the north side of the simplified city is further amplified as it interacts with the forward-flank gust front (Figure 6f). The primary updraft has also moved closer to the area of higher CAPE air within the simplified city (Figure 6h). From a previous analysis (Figures 3c and 5b), this is approximately the time that the supercell in the city simulation begins experiencing a larger UH_{0-1} relative to the control simulation.

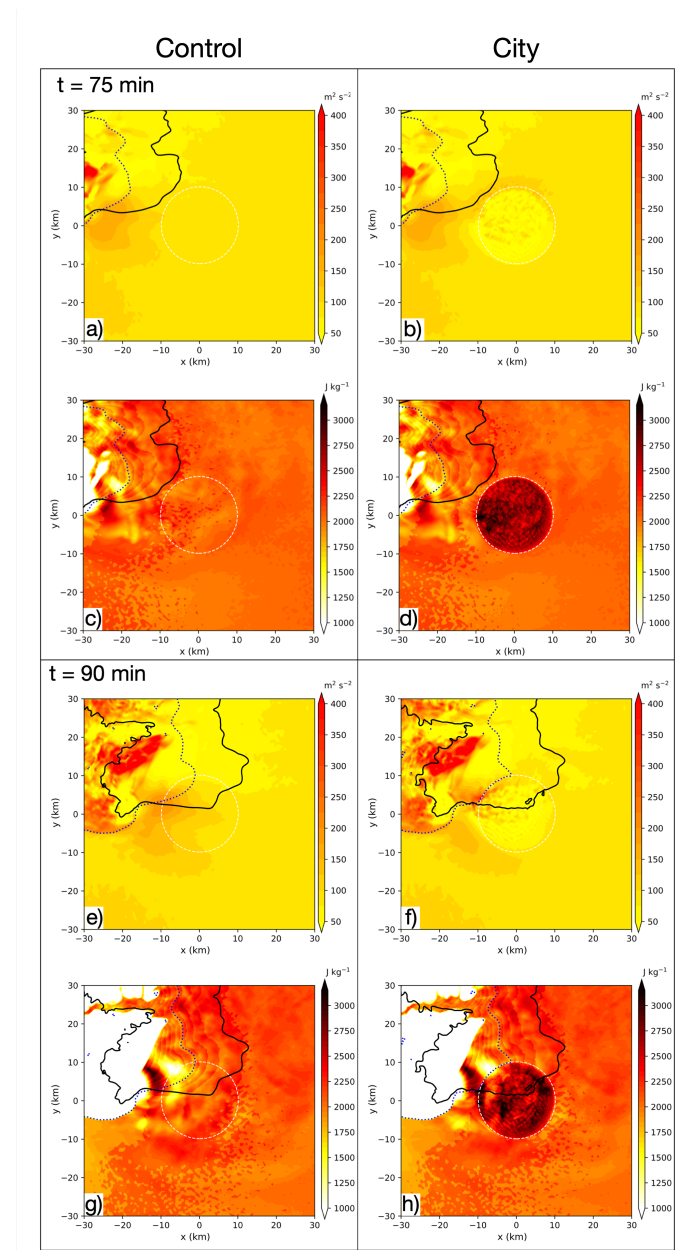


Figure 6. Storm relative helicity (integrated from 0 to 1 km; panels (a,b,e,f)) and surface-based convective available potential energy (c,d,g,h) at $t = 75$ min and $t = 90$ min in the control and city simulations. The solid black line in each panel represents the $2 g kg^{-1}$ contour of the rain water mixing ratio at $z = 25$ m, the dotted blue line is the $-1 K$ potential temperature perturbation at $z = 25$ m (to estimate the storm gust front), and the dashed white line indicates the areal extent of the ideal city. In the control simulations (a,c,e,g), the areal extent of the city is shown only for reference.

Figure 7 provides an in-depth comparison of the low-level structure in the two simulations at two different times. At $t = 93$ min, the storms in the two different simulations are very similar in numerous ways. The primary updraft is centered approximately 12–13 km west of the domain center with the surface gust front underneath the main updraft. A

prominent appendage is seen in the precipitation field near $x = -18$ km, $y = -2$ km and the strongest surface winds behind the surface gust front are from the northwest. The most noticeable differences are found within the inflow and forward flank regions. In the city simulation (Figure 7b), the inflow winds near the surface have a more southerly component compared to the control simulation. To the east of the primary updraft (near $x = -5$ km, $y = 2.5$ km), there is a stronger directional wind shift in the city simulation, which is also very near the area of enhanced 0–1 km SRH seen in Figure 6f. The supercell in the city simulation also possesses areas of stronger UH_{2-5} as well as pockets of UH_{0-1} along the forward flank gust front that are not present in the control simulation. At $t = 121$ min, the supercell in the city simulation is exiting the eastern edge of the city (Figure 7d). Two prominent ‘kinks’ in the gust front are present in the city simulation, both of which contain areas of enhanced UH_{0-1} . No large values of UH_{0-1} are present along the gust front of the supercell in the control simulation. In fact, the area of largest UH_{0-1} UH is well behind the gust front and outside of the primary updraft.

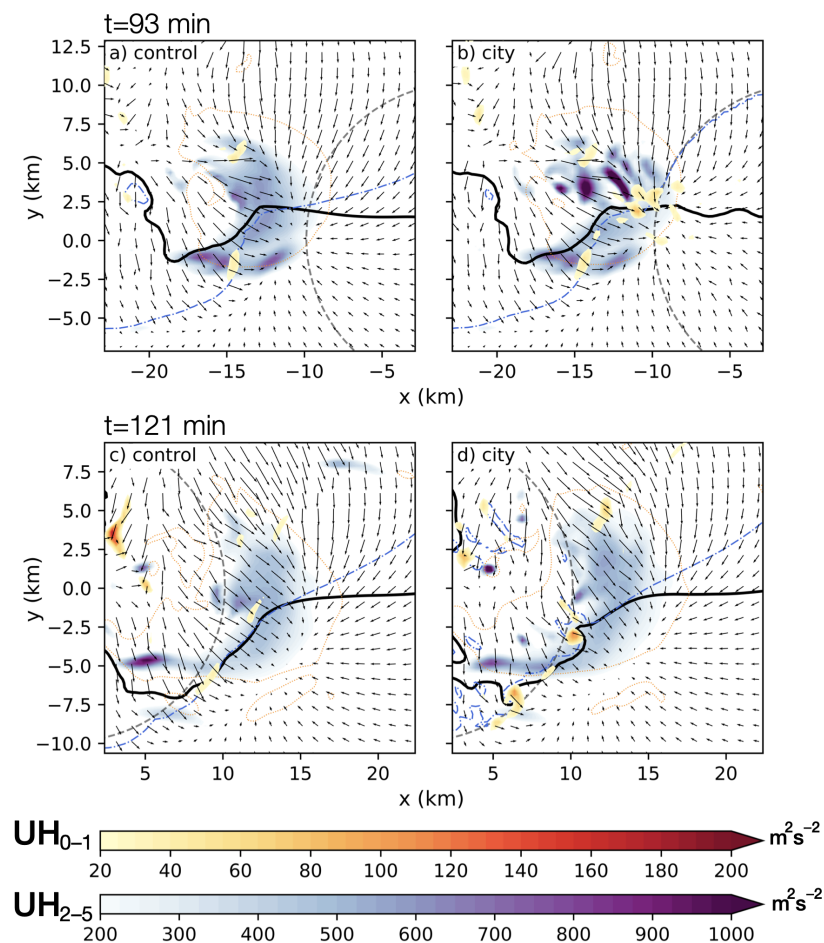


Figure 7. Overview of the storm structure at $t = 93$ min (top) and $t = 121$ min (bottom). The solid black line is the 2 g kg^{-1} contour of the rain water mixing ratio at $z = 25$ m, the dashed blue line is the -1 K potential temperature perturbation at $z = 25$ m (to estimate the storm gust front), the thin, dashed orange line is the 10 m s^{-1} contour of vertical velocity at $z = 6$ km, and the arrows represents the wind vectors at $z = 25$ m. The filled cool colors are 2–5 km updraft helicity and the filled warm colors are 0–1 km updraft helicity. Values are filtered to only show 0–1 km UH values at the grid points with 2–5 km UH greater or equal to $150 \text{ m}^2 \text{ s}^{-2}$. The dashed gray circle represents the location and extent of the idealized city.

The presence of the simplified city also results in increased downwind precipitation, which is one of the most commonly documented signatures of city–storm interac-

tions [29,30,49]. Figure 8a shows swaths of accumulated rainfall at the lowest model grid level. On the western half of the domain ($x < 0$ km), the two simulations produce strikingly similar results. However, differences become apparent as the supercells track through the eastern half of the domain ($x > 0$ km). The strongest enhancement appears approximately 10–60 km downwind of the city center. There is also evidence of increased hail, with the largest differences occurring between $x = 30$ km and $x = 45$ km. A similar increase in hail was documented in the squall line simulations of [33].

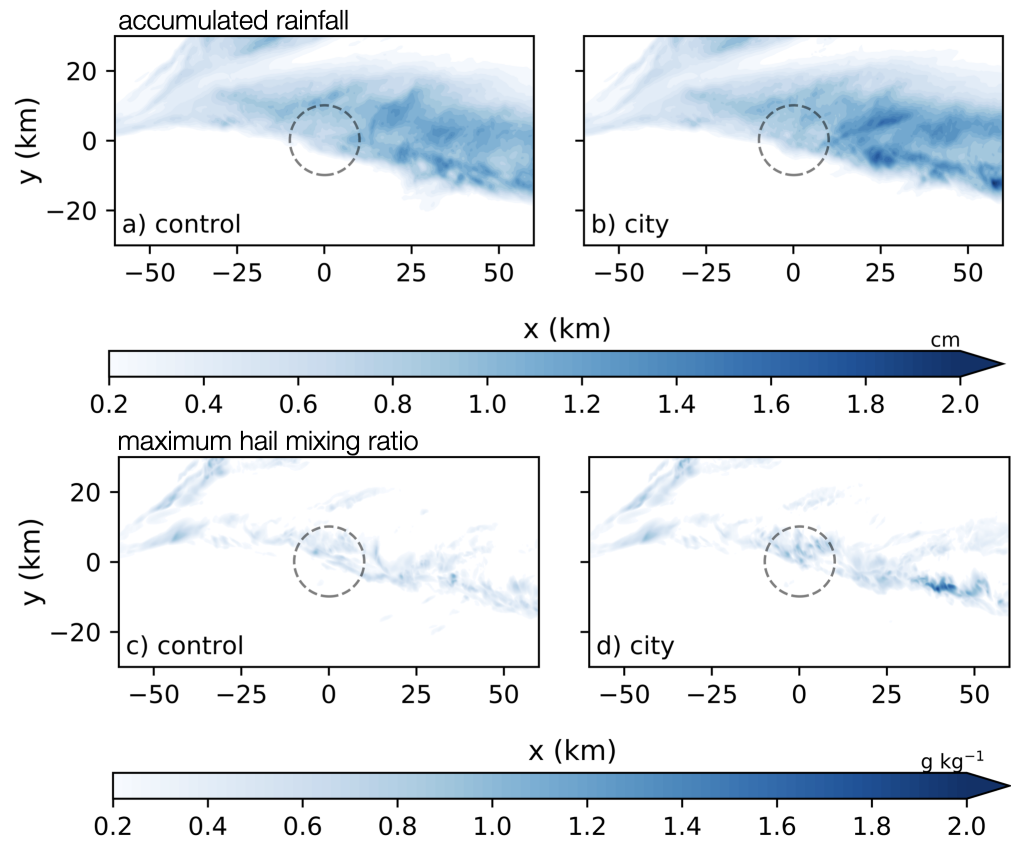


Figure 8. Swaths of accumulated surface rainfall (top) and maximum grid point hail mixing ratio at the lowest model level (bottom). The dashed gray circle represents the location and extent of the idealized city.

To further examine which aspects of the simplified city are most responsible for the observed variations in low-level mesocyclone strength, two additional simulations are presented for comparison to the city and control simulations. In one simulation (herein referred to as the “noUHI” simulation), the simplified city does not produce a heat island but still represents an area of enhanced surface roughness length. In the second simulation, (herein referred to as “no Δz_0 ”), a heat island is present but the surface roughness length is not enhanced over the simplified city. At midlevels, UH_{2-5} is similar among all four simulations prior to $t = 100$ min (Figure 9). The supercell in each of the four simulations experiences a local maximum of over $2500 \text{ m}^2 \text{ s}^{-2}$ at approximately $t = 97$ min. After this time, UH_{2-5} decreases in all simulations; however, the decrease between $t = 100$ min and $t = 115$ min in noUHI more closely aligns with the control simulation, while the decrease in no Δz_0 closely resembles that of the city simulation. The city and no Δz_0 simulations have values of UH_{2-5} that are occasionally more than double those in control and noUHI. After $t = 115$ min, UH_{2-5} in the four simulations exhibits a similar cyclic pattern with the noUHI simulation tending to have slightly larger values than the other three simulations. Closer to the surface, UH_{0-1} in the noUHI simulation is substantially less than in the city simulation from $t = 100$ – 120 min and follows a pattern that is very similar to that of the control

simulation, whereas $\text{no}\Delta z_0$ closely resembles the city simulation (Figure 9b). While passing over the simplified city, the maximum low-level vertical velocity values in the control and noUHI simulations are less than those in the city and $\text{no}\Delta z_0$ simulations (Figure 9c,d). This is almost assuredly due to the enhanced CAPE values in the city (Figure 6d) and $\text{no}\Delta z_0$ simulations (not shown). NM23 have previously shown that air parcels originating over a heat island with enhanced CAPE are ingested by the convective updrafts leading to enhanced buoyant acceleration.

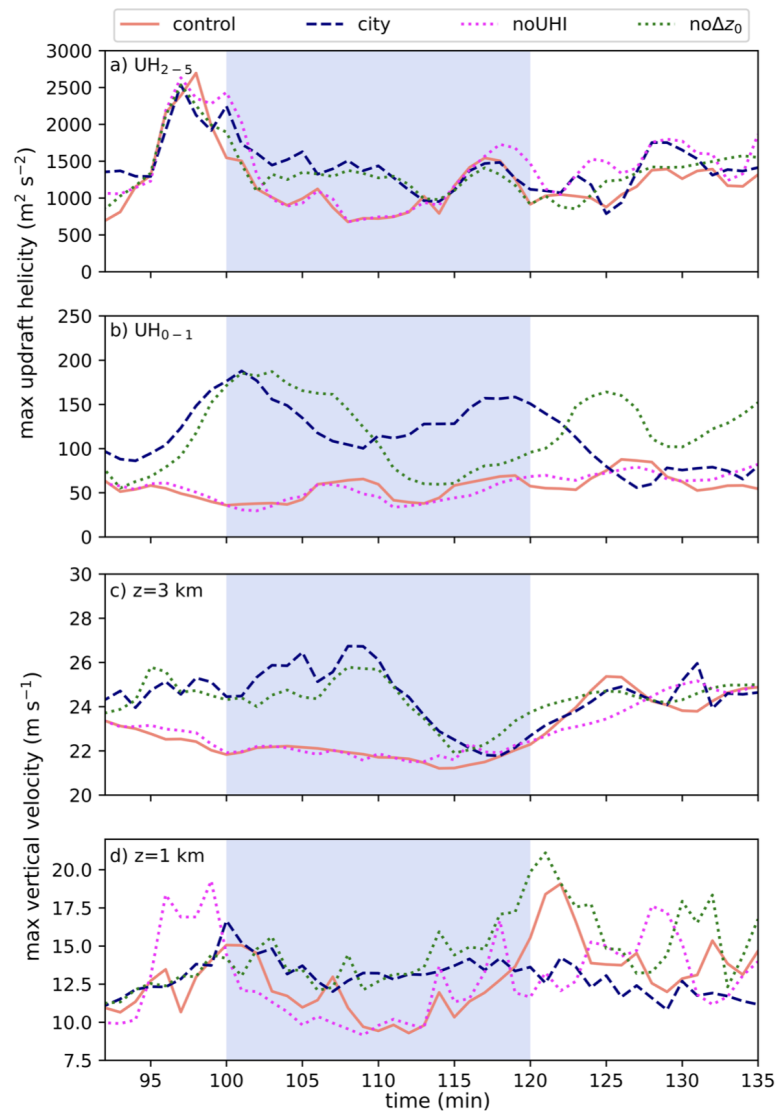


Figure 9. (a) Time-series of grid point maximum updraft helicity from 2 to 5 km in the control (solid orange line), city (dashed blue line), noUHI (dotted magenta line), and $\text{no}\Delta z_0$ (dashed green line) simulations. The shaded blue area indicates the approximate time period in which the updraft of the right-moving supercell is interacting with the idealized city. (b) Same as (a), except showing 0–1 km updraft helicity. Values in (b) are smoothed using a 5 min moving average and masked to only consider grid points also associated with UH_{2-5} greater than $150 \text{ m}^2 \text{ s}^{-2}$. Panels (c,d) show time series of maximum vertical velocity at 3 km and 1 km, respectively. Notation is the same as in panels (a,b).

The heat island also appears to be the primary driver of variations in storm relative helicity between the different simulations. Figure 10 shows the difference in 0–1 km SRH in the noUHI simulation compared to the control and city simulations at $t = 75 \text{ min}$. Compared to the control simulation, 0–1 km SRH values are slightly larger (approximately

10%) over the area where the surface roughness length is increased. In addition, while 0–1 km SRH values in noUHI are substantially larger in the center of the domain compared to the city simulation, there is no ribbon of enhanced 0–1 km SRH on the north side of the simplified city. However, despite the larger SRH over the entirety of the simplified city, the supercell in noUHI does not experience enhanced UH_{0-1} like the supercell in the city simulation (Figure 9b). Based on this evidence it appears that the larger UH_{0-1} in the city simulation from $t = 100$ min to $t = 120$ min is more influenced by the stronger low-level updrafts—which are a result of the storm ingesting warm, buoyant air originating from the heat island—than by the magnitude of 0–1 km SRH over the city.

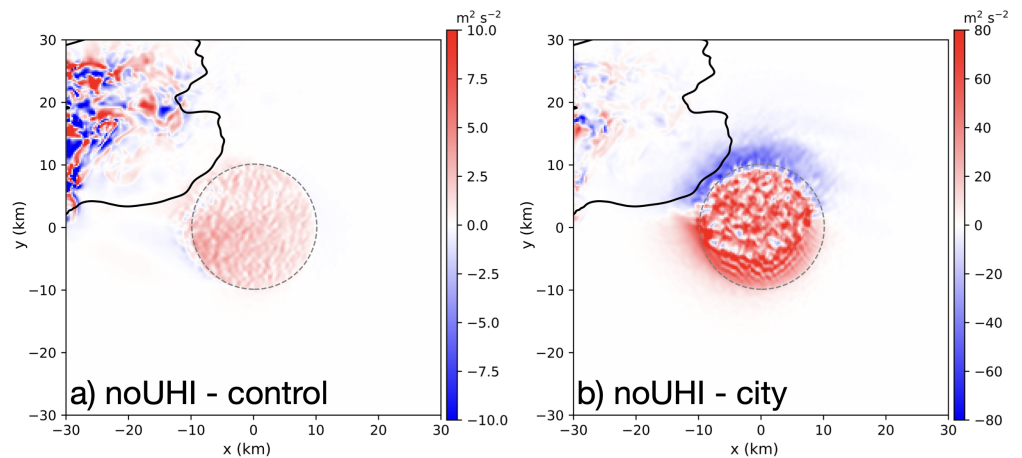


Figure 10. Difference in 0–1 km SRH at $t = 75$ min between (a) noUHI and control and (b) noUHI and city. The solid black line is the 2 g kg^{-1} contour of the rain water mixing ratio at $z = 25$ m in the noUHI simulation and the dashed gray line represents the horizontal extent of the idealized city.

Several sensitivity tests are presented in order to examine the robustness of the results. A small ensemble of simulations in which certain features of the simulations are slightly altered is shown in Table 2. The simulations are varied by changing the microphysics parameterization, enabling a radiation parameterization, and shifting the location of the initial warm bubble perturbation. In the control_rad and city_rad simulations, the short-wave radiation parameterization is configured with a fixed latitude and longitude of 38.32° N , -85.75° W and a simulation start time of 16 UTC on 15 July. While the fine-scale details in each of these simulations vary slightly, the overall findings remain unchanged. Figure 11 shows that, in all sensitivity tests, both the maximum UH_{0-1} magnitude and overall area of UH_{0-1} are greater in the simulation with a city than in the appropriate comparison control simulation during the 20 min period when the storms pass over the simplified city. All of the city simulations exhibit similar characteristics beyond the patterns in UH_{0-1} , such as strengthened low-level updrafts while passing over the simplified city, enhanced precipitation downwind of the city, and a ribbon of larger 0–1 km SRH on the northern edge of the simplified city (not shown).

Table 2. Summary of sensitivity experiments. All simulations are identical to the control and city simulations discussed in Section 2 except in the specific manner described in the second column.

Name	Description
control_rad	Short-wave and long-wave radiation are parameterized using the NASA Goddard scheme [50,51].
city_rad	

Table 2. Cont.

Name	Description
control_nssl city_nssl	Microphysics are represented using the NSSL double-moment scheme [52].
control_west city_west	Initial warm bubble perturbation is shifted 5 km to the west.
city_pert	Skin temperature perturbation is set to 5.2 K and surface roughness length over the city is 2.1 m.

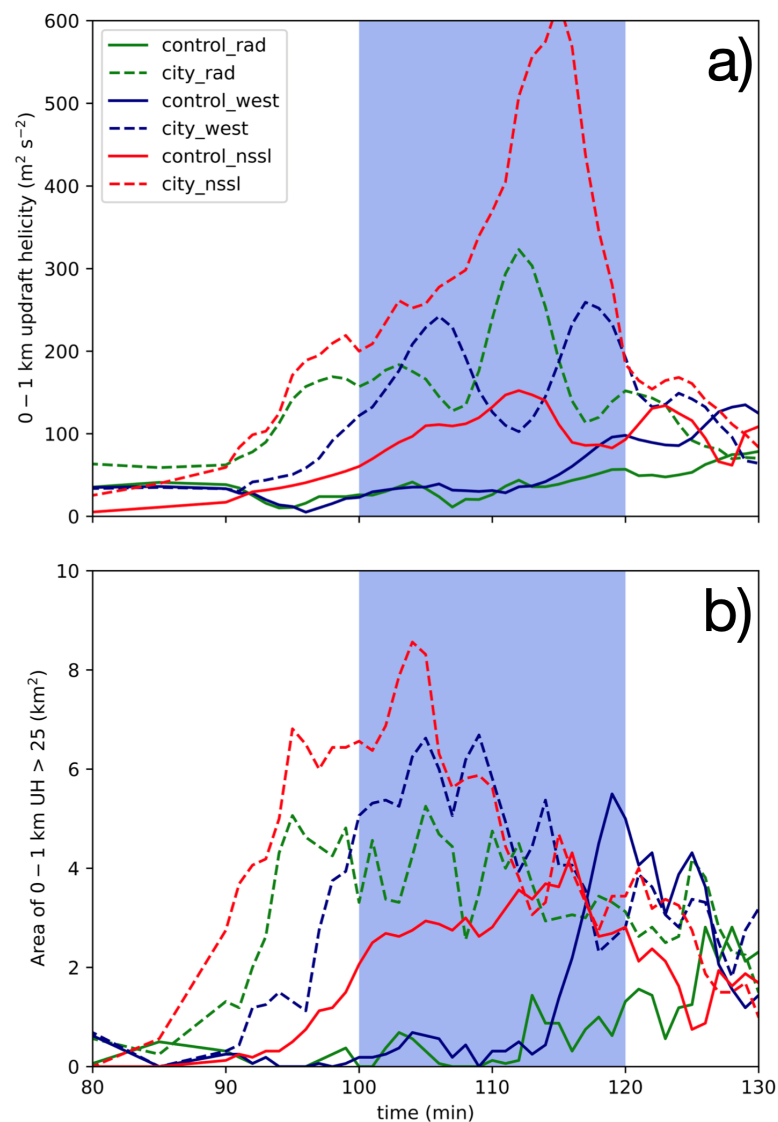


Figure 11. Time-series analysis of (a) maximum of 0–1 km updraft helicity and (b) areal extent of 0–1 km updraft helicity greater than $25 \text{ m}^2 \text{ s}^{-2}$ in the sensitivity tests described in Table 2. The city_pert simulation is not included in this figure because the results were very similar to the city simulation. Values after $t = 90 \text{ min}$ in (a) are smoothed using a 5 min moving average. All values in (a,b) are masked to only consider grid points that are also associated with UH_{2-5} greater than $150 \text{ m}^2 \text{ s}^{-2}$.

4. Summary and Conclusions

An idealized cloud model is used to examine the behavior of a supercell thunderstorm interacting with a simplified urban area, characterized by enhanced surface temperature and roughness length relative to its surroundings. These results are compared to those from a control simulation without a city. The results show that the city has substantial influence on the properties of the supercell's rotating updraft, primarily near the surface. The simulation with a simplified city produces a supercell with a stronger low-level updraft and enhanced updraft helicity beginning near the upwind edge of the city and continuing past the downwind side. These differences are likely related to modifications to the near-storm environment, including increases in CAPE over the city and the presence of a narrow band of a larger 0–1 km SRH on the northern side of the city. Additionally, the supercell that interacts with the city also produces more rain and hail than the supercell in the control simulation. This is consistent with many previous findings of precipitation enhancement downwind of an urban area. Additional simulations are shown in which the city is characterized by either enhanced surface roughness length or a heat island. The supercell in the enhanced roughness length simulation evolves in a similar manner to the control simulation and does not experience the strong increase in UH_{0-1} that is seen in the city simulation. In contrast, the supercell in the simulation with a heat island and no roughness length gradient experiences enhanced low-level updrafts and an increase in UH_{0-1} similar to the storm in the city simulation. This suggests that the urban heat island may have a stronger impact on updraft helicity enhancement than horizontal gradients in surface roughness length.

While previous studies have shown that cities can have an impact on atmospheric convection, this current study presents evidence that large urban areas with prominent heat islands may alter rotational characteristics—and perhaps a tornado producing potential—of supercells. Future work will focus on examining modifications to storm-scale processes—particularly those that may influence the development of vertical vorticity near the surface—that result in enhanced updraft helicity when the supercell interacts with a city.

Author Contributions: Conceptualization, J.N.; methodology, J.N.; software, J.N., M.E.B. and E.G.G.; formal analysis, J.N., M.E.B. and E.G.G.; writing—original draft preparation, M.E.B. and E.G.G.; writing—review and editing, J.N.; visualization, J.N., M.E.B. and E.G.G.; supervision, J.N.; project administration, J.N.; funding acquisition, J.N. All authors have read and agreed to the published version of the manuscript.

Funding: This research was sponsored by the National Science Foundation grant AGS-1953791.

Data Availability Statement: The numerical model used in this study (CM1) is freely available to download from <https://www2.mmm.ucar.edu/people/bryan/cm1/> (accessed on 18 December 2023). The modified version of CM1 used in this study, along with the appropriate model namelist, is available for download at <https://doi.org/10.6084/m9.figshare.22312066.v1> (accessed on 18 December 2023).

Acknowledgments: All simulations were carried out on the Cheyenne supercomputer (doi:10.5065/D6RX99HX) provided by NCAR's Computational and Information Systems Laboratory, sponsored by the National Science Foundation. We thank George Bryan for developing and maintaining CM1. We would also like to thank Larissa Reames for many helpful discussions that helped guide this research.

Conflicts of Interest: The authors declare no conflicts of interest.

References

1. Smith, B.T.; Thompson, R.L.; Grams, J.S.; Broyles, C.; Brooks, H.E. Convective modes for significant severe thunderstorms in the contiguous United States. Part I: Storm classification and climatology. *Weather Forecast* **2012**, *27*, 1114–1135. [[CrossRef](#)]
2. Weisman, M.L.; Klemp, J.B. The dependence of numerically simulated convective storms on vertical wind shear and buoyancy. *Mon. Weather Rev.* **1982**, *110*, 504–520. [[CrossRef](#)]
3. Weisman, M.L.; Klemp, J.B. The structure and classification of numerically simulated convective storms in directionally varying wind shears. *Mon. Weather Rev.* **1984**, *112*, 2479–2498. [[CrossRef](#)]

4. Rasmussen, E.N.; Blanchard, D.O. A baseline climatology of sounding-derived supercell and tornado forecast parameters. *Weather Forecast* **1998**, *13*, 1148–1164. [[CrossRef](#)]
5. Thompson, R.L.; Edwards, R.; Hart, J.A.; Elmore, K.L.; Markowski, P. Close proximity soundings within supercell environments obtained from the Rapid Update Cycle. *Weather Forecast* **2003**, *18*, 1243–1261. [[CrossRef](#)]
6. Atkins, N.T.; Weisman, M.L.; Wicker, L.J. The influence of preexisting boundaries on supercell evolution. *Mon. Weather Rev.* **1999**, *127*, 2910–2927. [[CrossRef](#)]
7. Richardson, Y.P.; Droegemeier, K.K.; Davies-Jones, R.P. The influence of horizontal environmental variability on numerically simulated convective storms. Part I: Variations in vertical shear. *Mon. Weather Rev.* **2007**, *135*, 3429–3455. [[CrossRef](#)]
8. Ziegler, C.L.; Mansell, E.R.; Straka, J.M.; Macgorman, D.R.; Burgess, D.W. The impact of spatial variations of low-level stability on the life cycle of a simulated supercell storm. *Mon. Weather Rev.* **2010**, *138*, 1738–1766. [[CrossRef](#)]
9. Coffey, B.E.; Parker, M.D. Impacts of increasing low-level shear on supercells during the early evening transition. *Mon. Weather Rev.* **2015**, *143*, 1945–1969. [[CrossRef](#)]
10. Davenport, C.E.; Parker, M.D. Impact of environmental heterogeneity on the dynamics of a dissipating supercell thunderstorm. *Mon. Weather Rev.* **2015**, *143*, 4244–4277. [[CrossRef](#)]
11. Magee, K.M.; Davenport, C.E. An observational analysis quantifying the distance of supercell-boundary interactions in the great plains. *J. Oper. Meteorol.* **2020**, *8*, 15–38. [[CrossRef](#)]
12. Davenport, C.E. Environmental evolution of long-lived supercell thunderstorms in the Great Plains. *Weather Forecast* **2021**, *36*, 2187–2209. [[CrossRef](#)]
13. Fischer, J.; Dahl, J.M.L. Supercell-External Storms and Boundaries Acting as Catalysts for Tornadogenesis. *Mon. Weather Rev.* **2023**, *151*, 23–38. [[CrossRef](#)]
14. Markowski, P.M.; Dotzek, N. A numerical study of the effects of orography on supercells. *Atmos. Res.* **2011**, *100*, 457–478. [[CrossRef](#)]
15. Scheffknecht, P.; Serafin, S.; Grubišić, V. A long-lived supercell over mountainous terrain. *Q. J. R. Meteorol. Soc.* **2017**, *143*, 2973–2986. [[CrossRef](#)]
16. Mulholland, J.P.; Nesbitt, S.W.; Trapp, R.J. A case study of terrain influences on upscale convective growth of a supercell. *Mon. Weather Rev.* **2019**, *147*, 4305–4324. [[CrossRef](#)]
17. Mulholland, J.P.; Nesbitt, S.W.; Trapp, R.J.; Peters, J.M. The influence of terrain on the convective environment and associated convective morphology from an idealized modeling perspective. *J. Atmos. Sci.* **2020**, *77*, 3929–3949. [[CrossRef](#)]
18. Tang, B.; Vaughan, M.; Lazear, R.; Corbosiero, K.; Bosart, L.; Wasula, T.; Lee, I.; Lipton, K. Topographic and boundary influences on the 22 May 2014 Duanesburg, New York, tornadic supercell. *Weather Forecast* **2016**, *31*, 107–127. [[CrossRef](#)]
19. Elsner, J.B.; Fricker, T.; Widen, H.M.; Castillo, C.M.; Humphreys, J.; Jung, J.; Rahman, S.; Richard, A.; Jagger, T.H.; Bhatrasat-aponkul, T.; et al. The relationship between elevation roughness and tornado activity: A spatial statistical model fit to data from the central great plains. *J. Appl. Meteorol. Climatol.* **2016**, *55*, 849–859. [[CrossRef](#)]
20. Lyza, A.W.; Knupp, K.R. A background investigation of tornado activity across the Southern Cumberland Plateau Terrain system of Northeastern Alabama. *Mon. Weather Rev.* **2018**, *146*, 4261–4278. [[CrossRef](#)]
21. Hua, Z.; Chavas, D.R. The empirical dependence of tornadogenesis on elevation roughness: Historical record analysis using Bayes’s law in Arkansas. *J. Appl. Meteorol. Climatol.* **2019**, *58*, 401–411. [[CrossRef](#)]
22. Houser, J.B.; McGinnis, N.; Butler, K.M.; Bluestein, H.B.; Snyder, J.C.; French, M.M. Statistical and empirical relationships between tornado intensity and both topography and land cover using rapid-scan radar observations and a GIS. *Mon. Weather Rev.* **2020**, *148*, 4313–4338. [[CrossRef](#)]
23. Kellner, O.; Niyogi, D. Land surface heterogeneity signature in tornado climatology? An illustrative analysis over Indiana, 1950–2012. *Earth Interact.* **2014**, *18*, 1–32. [[CrossRef](#)]
24. Markert, A.; Griffin, R.; Knupp, K.; Molthan, A.; Coleman, T. A spatial pattern analysis of land surface roughness heterogeneity and its relationship to the initiation of weak tornadoes. *Earth Interact.* **2019**, *23*, 1–28. [[CrossRef](#)]
25. Schenkman, A.D.; Xue, M.; Hu, M. Tornadogenesis in a high-resolution simulation of the 8 May 2003 Oklahoma City supercell. *J. Atmos. Sci.* **2014**, *71*, 130–154. [[CrossRef](#)]
26. Roberts, B.; Xue, M.; Schenkman, A.D.; Dawson, D.T. The role of surface drag in tornadogenesis within an idealized supercell simulation. *J. Atmos. Sci.* **2016**, *73*, 3371–3395. [[CrossRef](#)]
27. Fiedler, B.H. Axisymmetric tornado simulations with a semi-slip boundary. *Fluids* **2017**, *2*, 68. [[CrossRef](#)]
28. Huff, F.A.; Changnon, S.A. Climatological assessment of urban effects on precipitation at St. Louis. *J. Appl. Meteorol.* **1972**, *11*, 823–842. [[CrossRef](#)]
29. Huff, F.A.; Changnon, S.A. Precipitation modification by major urban areas. *Bull. Am. Meteorol. Soc.* **1973**, *54*, 1220–1232. [[CrossRef](#)]
30. Shepherd, J.M.; Pierce, H.; Negri, A.J. Rainfall modification by major urban areas: Observations from spaceborne rain radar on the TRMM satellite. *J. Appl. Meteorol.* **2002**, *41*, 689–701. [[CrossRef](#)]
31. Niyogi, D.; Pyle, P.; Lei, M.; Arya, S.P.; Kishtawal, C.M.; Shepherd, M.; Chen, F.; Wolfe, B. Urban modification of thunderstorms: An observational storm climatology and model case study for the Indianapolis urban region. *J. Appl. Meteorol. Climatol.* **2011**, *50*, 1129–1144. [[CrossRef](#)]
32. Naylor, J. Idealized simulations of city-storm interactions in a two-dimensional framework. *Atmosphere* **2020**, *11*, 707. [[CrossRef](#)]

33. Naylor, J.; Mulholland, J.P. The Impact of Vertical Wind Shear on the Outcome of Interactions Between Squall Lines and Cities. *J. Geophys. Res. Atmos.* **2023**, *128*, e2022JD037237. [[CrossRef](#)]
34. Reames, L.J.; Stensrud, D.J. Influence of a Great Plains urban environment on a simulated supercell. *Mon. Weather Rev.* **2018**, *146*, 1437–1462. [[CrossRef](#)]
35. Lin, Y.; Fan, J.; Jeong, J.H.; Zhang, Y.; Homeyer, C.R.; Wang, J. Urbanization-induced land and aerosol impacts on storm propagation and hail characteristics. *J. Atmos. Sci.* **2021**, *78*, 925–947. [[CrossRef](#)]
36. Bryan, G.H.; Fritsch, J.M. A benchmark simulation for moist nonhydrostatic numerical models. *Mon. Weather Rev.* **2002**, *130*, 2917–2928. [[CrossRef](#)]
37. Dahl, J.M. Near-ground rotation in simulated supercells: On the robustness of the baroclinic mechanism. *Mon. Weather Rev.* **2015**, *143*, 4929–4942. [[CrossRef](#)]
38. Dawson, D.T.; Xue, M.; Shapiro, A.; Milbrandt, J.A.; Schenkman, A.D. Sensitivity of real-data simulations of the 3 May 1999 Oklahoma City tornadic supercell and associated tornadoes to multimoment microphysics. Part II: Analysis of buoyancy and dynamic pressure forces in simulated tornado-like vortices. *J. Atmos. Sci.* **2016**, *73*, 1039–1061. [[CrossRef](#)]
39. Boyer, C.H.; Dahl, J.M. The mechanisms responsible for large near-surface vertical vorticity within simulated supercells and quasi-linear storms. *Mon. Weather Rev.* **2020**, *148*, 4281–4297. [[CrossRef](#)]
40. Morrison, H.; Curry, J.A.; Khvorostyanov, V.I. A new double-moment microphysics parameterization for application in cloud and climate models. Part I: Description. *J. Atmos. Sci.* **2005**, *62*, 1665–1677. [[CrossRef](#)]
41. Morrison, H.; Thompson, G.; Tatarskii, V. Impact of cloud microphysics on the development of trailing stratiform precipitation in a simulated squall line: Comparison of one- and two-moment schemes. *Mon. Weather Rev.* **2009**, *137*, 991–1007. [[CrossRef](#)]
42. Fairall, C.W.; Bradley, E.F.; Hare, J.E.; Grachev, A.A.; Edson, J.B. Bulk parameterization of air–sea fluxes: Updates and verification for the COARE algorithm. *J. Clim.* **2003**, *16*, 571–591. [[CrossRef](#)]
43. Donelan, M.A.; Haus, B.K.; Reul, N.; Plant, W.J.; Stiassnie, M.; Graber, H.C.; Brown, O.B.; Saltzman, E.S. On the limiting aerodynamic roughness of the ocean in very strong winds. *Geophys. Res. Lett.* **2004**, *31*, 1–5. [[CrossRef](#)]
44. Weisman, M.L.; Rotunno, R. The use of vertical wind shear versus helicity in interpreting supercell dynamics. *J. Atmos. Sci.* **2000**, *57*, 1452–1472. [[CrossRef](#)]
45. Kain, J.S.; Weiss, S.J.; Bright, D.R.; Baldwin, M.E.; Levit, J.J.; Carbin, G.W.; Schwartz, C.S.; Weisman, M.L.; Droegemeier, K.K.; Weber, D.; et al. Some practical considerations regarding horizontal resolution in the first generation of operational convection-allowing NWP. *Weather Forecast* **2008**, *23*, 931–952. [[CrossRef](#)]
46. Sobash, R.A.; Kain, J.S.; Bright, D.R.; Dean, A.R.; Coniglio, M.C.; Weiss, S.J. Probabilistic forecast guidance for severe thunderstorms based on the identification of extreme phenomena in convection-allowing model forecasts. *Weather Forecast* **2011**, *26*, 714–728. [[CrossRef](#)]
47. Naylor, J.; Gilmore, M.S.; Thompson, R.L.; Edwards, R.; Wilhelmson, R.B. Comparison of objective supercell identification techniques using an idealized cloud model. *Mon. Weather Rev.* **2012**, *140*, 2090–2102. [[CrossRef](#)]
48. Sobash, R.A.; Schwartz, C.S.; Romine, G.S.; Weisman, M.L. Next-day prediction of tornadoes using convection-allowing models with 1-km horizontal grid spacing. *Weather Forecast* **2019**, *34*, 1117–1135. [[CrossRef](#)]
49. Liu, J.; Niyogi, D. Meta-analysis of urbanization impact on rainfall modification. *Sci. Rep.* **2019**, *9*, 7301. [[CrossRef](#)]
50. Chou, M.D.; Suarez, M.J. *A Solar Radiation Parameterization for Atmospheric Studies*, NASA Tech Report; NASA Goddard Space Flight Center: Greenbelt, MD, USA, 1999.
51. Chou, M.D.; Suarez, M.J.; Liang, X.Z.; Yan, M.M.H.; Cote, C. *A Thermal Infrared Radiation Parameterization for Atmospheric Studies*, NASA Tech Report; NASA Goddard Space Flight Center: Greenbelt, MD, USA, 2001.
52. Mansell, E.R.; Ziegler, C.L.; Bruning, E.C. Simulated electrification of a small thunderstorm with two-moment bulk microphysics. *J. Atmos. Sci.* **2010**, *67*, 171–194. [[CrossRef](#)]

Disclaimer/Publisher’s Note: The statements, opinions and data contained in all publications are solely those of the individual author(s) and contributor(s) and not of MDPI and/or the editor(s). MDPI and/or the editor(s) disclaim responsibility for any injury to people or property resulting from any ideas, methods, instructions or products referred to in the content.